JOURNAL OF AIRCRAFT
Vol. 43, No. 5, September–October 2006

Unsteady Computational Investigations of Deploying Load Control Microtabs

Raymond Chow* and C. P. van Dam†
University of California, Davis, Davis, California 95616

DOI: 10.2514/1.22562

Flow around an airfoil with a deploying microtab device has been numerically simulated by solving the unsteady turbulent compressible Navier–Stokes equations with the OVERFLOW-2 solver. Using a Chimera/overset grid topology, microtabs were placed at 95% of chord of a symmetric NACA 0012 airfoil. Microtab heights on the order of 1% of chord, deployed on the order of one characteristic time unit were utilized. The unsteady effects of tab deployment time, deployment height, and freestream angle of attack on aerodynamic responses were also investigated. Validation studies with experimental results for static deployed microtabs and a dynamically deployed spoiler were also performed to ensure accurate temporal and spatial resolution of the numerical simulations.

Nomenclature

C_D	=	aerodynamic drag coefficient
C_L	=	aerodynamic lift coefficient
$C_{L,\text{adverse}}$	=	peak lift coefficient opposite in sense to the desired effect from device deployment
$C_{L,\text{retract}}$	=	nominal lift coefficient with retracted device
C_M	=	aerodynamic pitching moment coefficient about $c/4$ (nose-up positive)
C_P	=	pressure coefficient
c	=	main airfoil chord
DT	=	nondimensional time step
$h(T)$	=	tab position at time T
h_{tab}	=	fully deployed tab height
T	=	nondimensional convective time (Ut/c)
T_{delay}	=	nondimensional time to peak adverse lift
T_{deploy}	=	nondimensional deployment time
$T_{50\%}$	=	nondimensional time to 50% of mean steady state lift
t	=	physical time (seconds)
U	=	freestream velocity
$v(T)$	=	tab velocity at time T
x	=	Cartesian coordinate
α	=	angle of attack (deg)
δ	=	normalized device position (0.00 when retracted, 1.00 when fully deployed)
θ	=	spoiler deployment angle

Introduction

ACTIVE load control devices have gained more and more attention in recent years as a viable technology as ubiquitous microelectronics have made sensors and control systems required for such devices more practical. Although the sensor and control systems have become feasible, much of the work on active load control devices has focused on systems that must still overcome many other technological hurdles and potentially impractical energy requirements. Small devices that affect the trailing edge flow such as Gurney flaps introduced by Liebeck [1] are more practical, but the small structural volumes of sharp trailing edge airfoils make the implementation of an actuation device difficult. To overcome many of these limitations, microtab devices have been proposed by Yen et al. [2,3] as a viable and effective concept for active load control applications. This concept involves small tabs that are placed ahead of the trailing edge of an airfoil and deploy approximately normal to the airfoil surface. These microtabs have a deployment height on the order of the boundary-layer thickness. The presence of the tabs changes the sectional camber and the trailing edge flow conditions as shown in Fig. 1, thereby affecting the aerodynamic characteristics of the section [4,5]. The engineering viability of these devices can be attributable to their mechanical simplicity and minimal structural intrusiveness. Arrays of these devices could be implemented, and investigations into the 3-D effects of these microtabs have been studied by Mayda et al. [6]. Based on this earlier work, microtabs have shown very promising potential without any foreseeable technological barriers.

To implement these devices, the unsteady behavior of these tabs must first be understood. The purpose of this study is to examine the transient behavior of deploying microtabs. The aerodynamic behavior of these microtabs will be simulated using computational fluid dynamics (CFD).

The major advantages of using CFD are twofold: first, it significantly reduces the cost of designing and constructing an experimental apparatus that is limited to one configuration; and secondly, CFD can provide detailed insight into the details of the flow physics that would be hidden in an experiment.

Methods

Flow Solver

OVERFLOW is a structured overset, Reynolds-averaged Navier–Stokes flow solver [7]. With its multi- and moving-body capabilities, OVERFLOW version 2 is particularly well suited for this study. As a flow solver, OVERFLOW-2 is very robust and comprehensive, allowing for the selection from a variety of numerical schemes, turbulence models, boundary conditions, and time advancement schemes [8]. Although various numerical methods are available in OVERFLOW-2, all calculations are performed with second-order central differencing using the approximate-factorized form of the Beam–Warming pentadiagonal scheme [9]. Whereas several 1- and 2-equation turbulence models are available, this study is limited to Menter's SST k–ω model [10] due to its superior performance for separated flows [11,12]. All solid boundaries are treated as viscous walls, and all calculations (except for the S809 validation cases) are performed fully turbulent. All unsteady calculations are performed

Presented as Paper 1063 at the 44th AIAA Aerospace Sciences Meeting and Exhibit, Reno, Nevada, 9–12 January 2006; received 19 January 2006; revision received 30 March 2006; accepted for publication 31 March 2006.

*Graduate Student Researcher, Department of Mechanical & Aeronautical Engineering, Student Member AIAA.

†Professor, Department of Mechanical & Aeronautical Engineering, Senior Member AIAA.

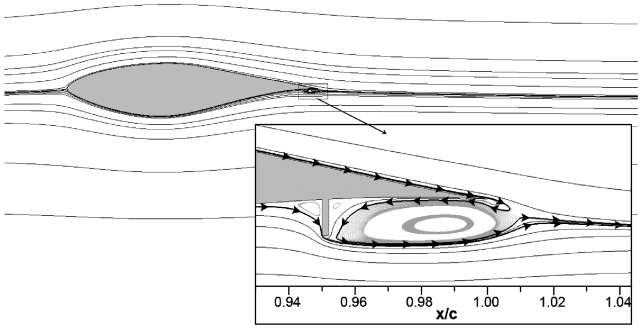

Fig. 1 Instantaneous streamlines of a S809 airfoil with a 1.10%c lower surface tab at 0.95c. Inset: Tab region with critical instantaneous streamlines denoted by arrows, $Ma = 0.25$, $Re = 1 \times 10^6$, $\alpha = 0$ deg.

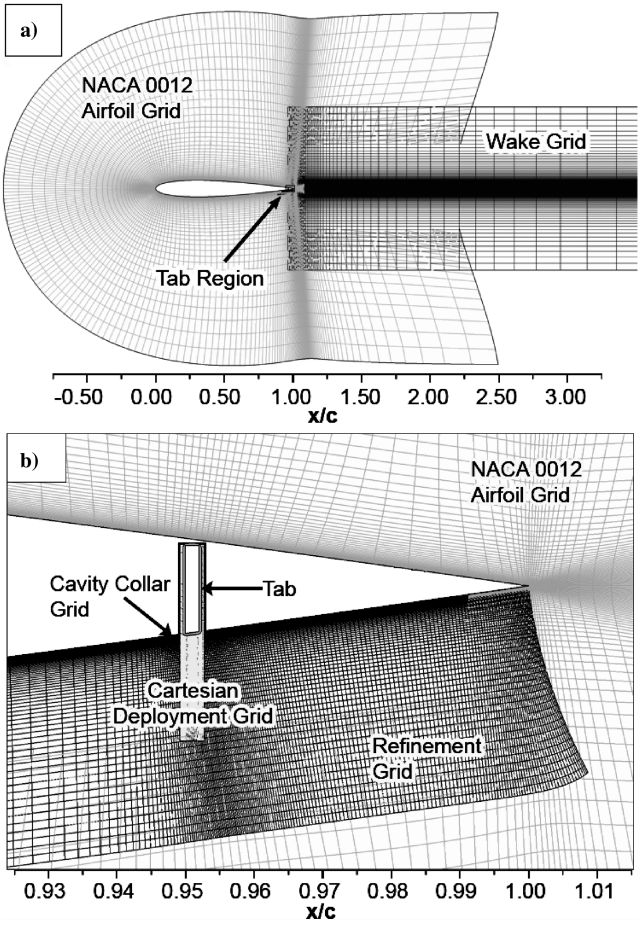

Fig. 2 Microtab grid system: a) near-body grids b) trailing edge tab region grids.

with second-order accuracy in time and with dual-time stepping [13,14].

Computational Meshes

The Chimera overset structured grid scheme is employed to model the computational flow domain. This approach allows geometrically complex multibody configurations to be constructed from sets of relatively simple overlapping body-fitted grids [15]. The near-body computational grid is generated with Chimera Grid Tools (CGT) 1.9 [16]. The CGT package contains independent grid generation, manipulation, visualization, and diagnosis tools that can be run in batch mode under the OVERGRID [17] graphical interface. All body-fitted grids were generated with a wall spacing of approximately $y^+ \approx 0.5$ [18]. The OVERFLOW-2 generated Cartesian off-body grid system ("BRICKS") consists of several levels of grid refinement extending to the boundary of the computational domain (approximately 50c), with a first level spacing on the order of the near-body outer boundary grid spacing [19]

The Chimera overset scheme is also well suited for moving body applications because body-fitted grids need only to be reconnected when the bodies are moved, rather than being regenerated. Human readable, XML input files are used to specify the prescribed motion of the bodies [20]. As the bodies move in the computational domain, surrounding grids are quickly and efficiently cut using Meakin's object X-Ray method [21] between each solution frame. Domain connectivity is also performed automatically by OVERFLOW-2 using nonconservative interpolation between overlapping grids.

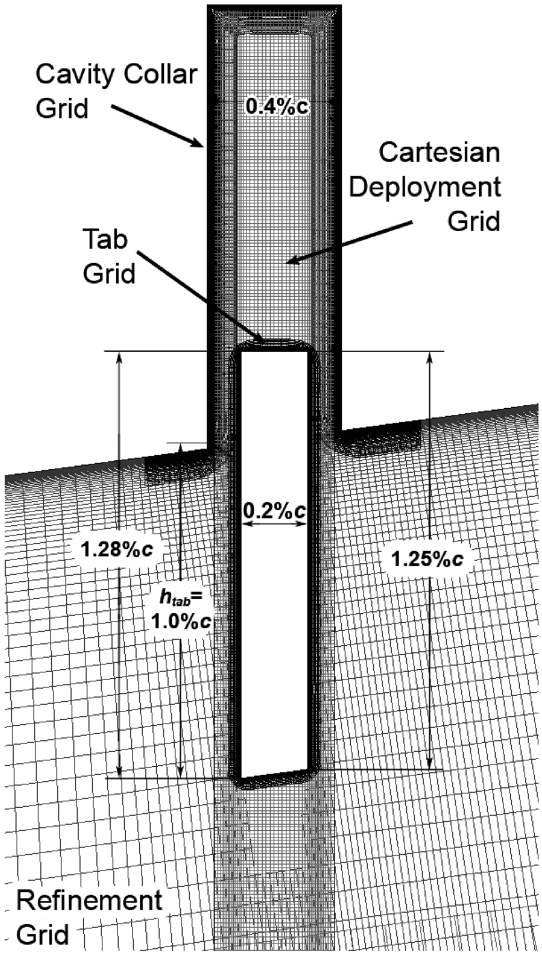

Fig. 3 Microtab grid for a 1.00%c tab deployment.

Microtab Grid Topology

The dynamic microtab geometry is built on a symmetric NACA 0012 airfoil. The 291×90 (streamwise $\times$ normal) C-type grid extends approximately 1.5c from the airfoil surface (Fig. 2a). The tab itself is constructed from a 1.25%c by 0.2%c rectangular body aligned normal to the mean camber line of the NACA 0012. The leading edge face of the tab is placed at 0.95c. The tip or lower surface of the tab is modified by aligning the foremost corner of the retracted tab flush to the surface of the airfoil and intersecting the two surfaces (Fig. 2b). The 269×14 O-type body-fitted tab grid extends approximately 0.2%c away from the tab (Fig. 3). The tab grid has a wall spacing of $y^+ \approx 0.5$, with a streamwise (surface direction) spacing on the order of y^+.

A 314×29 collar grid is used to define the geometry of the cavity around the tab. The cavity is 0.4%c wide and 1.329%c deep, creating a uniform 0.1%c gap between the cavity walls and the retracted tab. Inside the cavity and in the path of the tab, a 47×281 Cartesian grid with spacing the same as that of the tab grid's fringe cells, is generated. This "deployment" grid both helps to maintain a

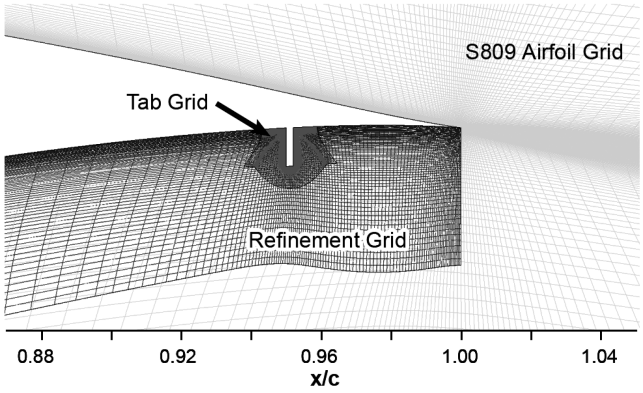

Fig. 4 Detailed grid of the S809 airfoil with fixed 1.10%c tab.

continuous domain in the cavity as the tab grid is deployed (by filling the vacated area) and to act as a highly refined first level off-body grid for the tab throughout the deployment phase.

A 183×74 refinement grid on the airfoil surface extending 5%c upstream and downstream of the tab and 2%c normal to the surface is also generated. This refinement grid, in addition to adding more points in the region of interest, also aids the transition between the highly refined spacing in the tab region and the coarser airfoil grid. A 183×57 Cartesian wake grid extending 5.5c downstream of the airfoil is also added. The far field is composed of Cartesian off-body grids (BRICKS) that extend approximately 50c away from the airfoil.

S809 Fixed Tab Grid Topology

An overset grid topology is also used to define the geometry of the fixed 1.1%c lower surface tab on the S809 airfoil (see Fig. 1 for overall geometry). Because the geometry did not contain any gaps, the near-body surface grid of the tab/airfoil could have been created as a single C-mesh grid. However, for consistency with the moving tab grid topology, overlapping overset grids are used to define the viscous surface geometry as well.

A traditional 299×125 C-type grid is used to define an unmodified S809 airfoil. The fixed tab geometry is created with a refined 118×79 collar grid that both defines the surface of the 1.10%c tab along with approximately 1%c of the airfoil surface up- and downstream of the tab. Similar to the microtab topology, a 114×112 refinement grid (over approximately the last 10%c of the airfoil lower surface and extending 4%c normal to the surface) acts both to improve grid resolution in the tab region and to help grid transition between the tab and airfoil (Fig. 4).

Deploying Spoiler Grid Topology

For the deploying spoiler study, the leading edge of a 10%c spoiler is located at 0.70c of a NACA 0012 airfoil. The upper surface of the spoiler is simply defined as a portion of the upper surface of the NACA 0012 airfoil from 0.70 to 0.80c. A part of the spoiler lower surface is defined by a horizontal plane that coincided with the NACA 0012 upper surface 0.80c. The nose is generated with a third-order polynomial that joined the two surfaces. The spoiler is discretized with a 142×100 C-type grid that extends a spoiler chord (10%c) away from the surface and 1.5 spoiler chords (15%c) into the wake. The cavity for the spoiler is generated so that a 0.1%c gap would remain between the cavity and retracted spoiler. Because of its size and smooth geometry, the spoiler cavity is integrated into the surface definition of the NACA 0012 airfoil. The 321×125 C-type grid used to create the modified NACA 0012 grid in this part of the study extends approximately 1.5c from the airfoil surface. The grid at three stages of spoiler deployment, post hole cutting, is shown in Fig. 5.

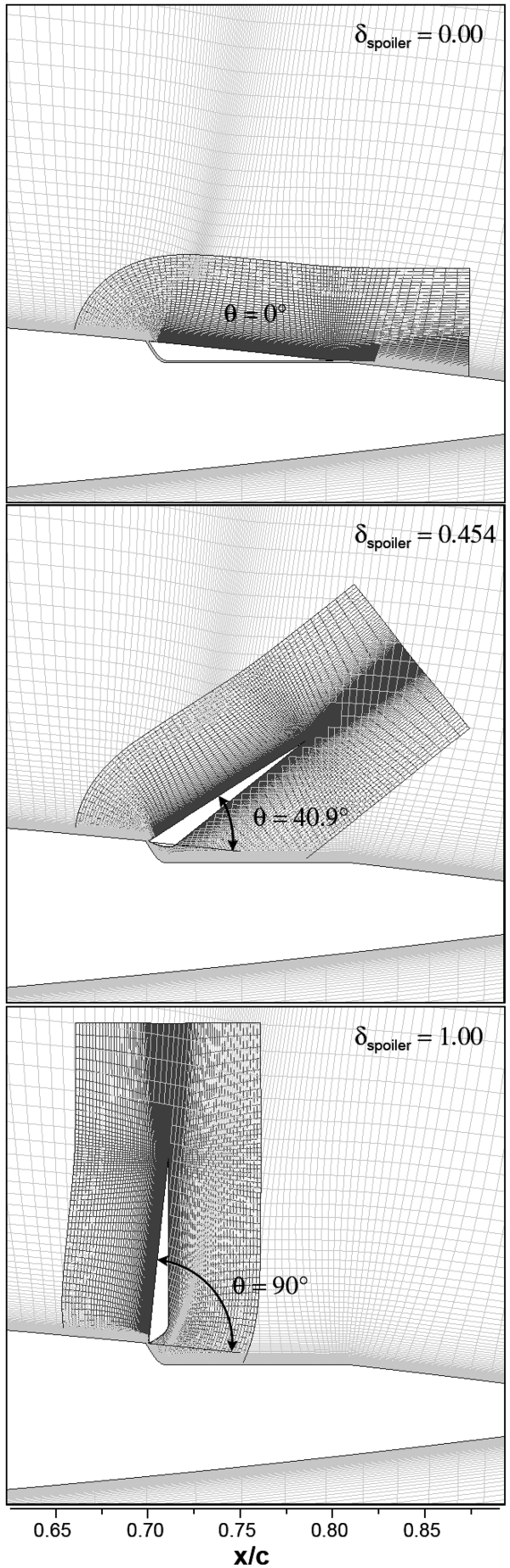

Fig. 5 Spoiler grid topology during deployment at three stations: retracted, intermediate ($\delta_{spoiler} = 0.454$), and fully deployed.

Dynamic Motion

Although all of the cases utilized the same tab grid with a length of $1.25\%c$, tab height was defined as the distance from a retracted (flush with the airfoil lower surface) position to the tip of the deployed tab, or effectively the vertical displacement distance. The microtabs were all deployed with a ramplike motion given by

$$h(T) = h_0 - (h_{\text{tab}}/2)\{1 - \cos[\pi(T - T_0)/(T_1 - T_0)]\} \quad (1)$$

where h_0 is the initial tab position, T_0 is the initial deployment time, and T_1 is the final deployment time. This ramp function leads to a simple sinusoidal velocity profile for deployment:

$$v(T) = -(h_{\text{tab}}/2)\frac{\pi}{(T_1 - T_0)}\sin[\pi(T - T_0)/(T_1 - T_0)] \quad (2)$$

All unsteady results are reported with the onset of motion as the start of time $T = 0$. The motion specification for the spoiler was very similar to the tab, differing only by replacing the translations with angular displacements. Only one spoiler deployment scenario was considered, using a fully deployed angle, θ_{spoiler} of 90 deg ($\delta_{\text{spoiler}} = 1.00$) and deployment time, T_{deploy} of 4.4, which was the baseline configuration in a study by Yeung et al. [22].

Numerical Validation

Because no time-accurate experimental results for deploying microtabs exist, direct validation of the computational results is not yet possible. OVERFLOW 2 and OVERFLOW-D have been extensively tested and validated against experimental results for store separation, rotorcraft, wind turbines, and other dynamic problems [23–26]. However, due to the relatively small geometry, significant overlapping viscous regions, and unsteady shedding created by the tabs it seemed prudent to perform a validation with similar flow physics. Fortunately, two published experimental data sets of very similar configurations do exist. The first is from an experiment of a fixed $1.1\%c$ microtab on the S809 airfoil by Baker et al. [27], as illustrated in Fig. 1. This data set provides an excellent case to ensure accuracy in the methods ability to capture microtab induced flow. The second is an unsteady, experiment of a rapidly deploying spoiler ($T_{\text{deploy}} = 4.4$) by Yeung et al. [22]. This spoiler case acts as an excellent benchmark for the selected methodology by validating the temporal accuracy, as well as including the rapidly changing geometry, interacting viscous regions, and unsteady separated flow. A previous computational study by Choi et al. [28] also used this rapidly deploying spoiler configuration provided additional data for comparison and validation. A grid convergence study performed on the microtab topology is discussed in the results.

Static Lower Surface Tab

Computationally, a Reynolds number (based on airfoil chord) of 1.0×10^6, and upper and lower surface transition at $0.02c$ and $0.05c$, respectively, were used to match experimental conditions [27]. However, to avoid incompressibility issues, the experimental Mach number of 0.17 was increased to 0.25. For stability, calculations were all started steady and restarted time accurately with 50 dual-time stepping subiterations and a time step $DT = 10^{-3}$. Solutions were run until oscillations were uniform and constant in the mean. Mean values are reported.

The lift and drag coefficients of the S809 with a static $1.1\%c$ tab are compared to experimental values in Fig. 6. For angles of attack from -2 to 8 deg computational results for lift and drag match almost exactly with experimental values. Unfortunately, beyond stall, no experimental drag data are available. Although lift is slightly overpredicted, there is still very good agreement on the onset and behavior of stall. The slight dip in the lift after the onset of stall is even seen computationally. Overall, there is excellent agreement with the experimental results.

Capturing the effects of the tab over such broad sweep of prestall angles of attack provides tremendous confidence in the ability of the methods to accurately capture the effects of the microtab itself over a range of boundary-layer thicknesses and trailing edge flow conditions. Although accurately capturing stall values would have been desirable, stall is an airfoil dominated effect. It is clear that from this study, microtab flow behavior can not only be qualitatively captured, but quantitatively predicted as well.

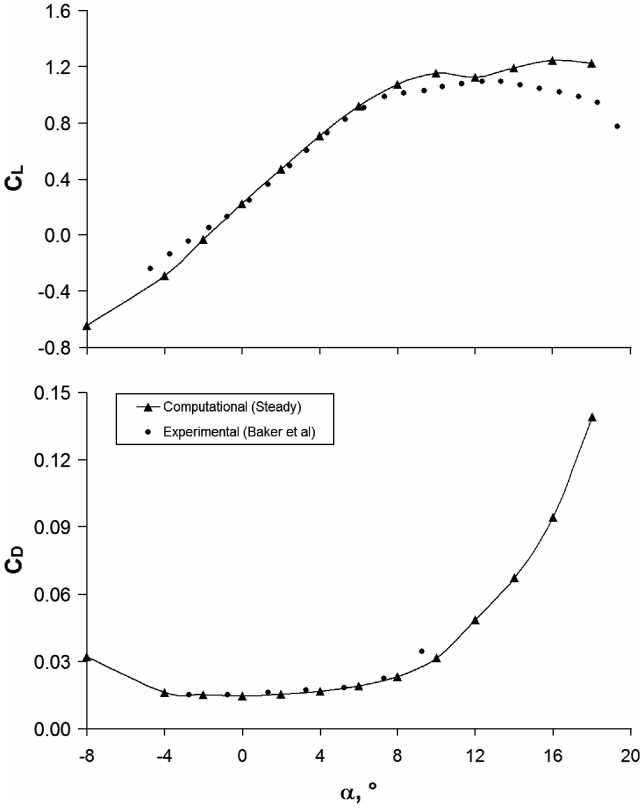

Fig. 6 Comparison of experimental and computational lift and drag for $1.10\%c$ fixed tab modified S809 airfoil at $Re = 1 \times 10^6$.

Rapidly Deploying Spoiler

A Reynolds number (based on airfoil chord length) of 3.5×10^5 was used, matching that of the experiment [22]. Like the static tab study, the freestream Mach number was increased to 0.25, from the 0.035 used in the experiment. This assumption was later shown to be valid, when a case run at Mach 0.035 using unsteady low-Mach preconditioning (that had not yet been implemented at the outset of this study) showed no visible differences in the solution in terms of the temporal evolution of the aerodynamic coefficients. The time-accurate calculation is started from a fully converged, steady solution over the airfoil and retracted spoiler. The solution is run time accurately for $1.0c/U$ before the spoiler motion is initiated to advect any transients associated with the change to time accuracy.

Results and Discussion

The lift, pitching moment, and drag coefficients of a deploying spoiler with a $0.1\%c$ hinge gap are compared to experimental results with a nominally $0.0\%c$ gap in Fig. 7. The instantaneous streamlines for various stages during deployment are shown in Fig. 8. The computational results compare reasonably well with experimental results. There is excellent agreement temporally and in the post deployment mean values.

As the spoiler deploys, a low pressure area from a strong vortex is created behind the spoiler. Initially, the effect of this low pressure region is almost completely canceled by an increase in pressure upstream of the spoiler. As the spoiler continues deployment and the size of the vortex grows and reaches the trailing edge of the airfoil, the peak adverse (in terms of desirable spoiler effect) lift and moment is reached.

The difference in drag before deployment is presumably due to some additional surface roughness or spacing gap in the retracted

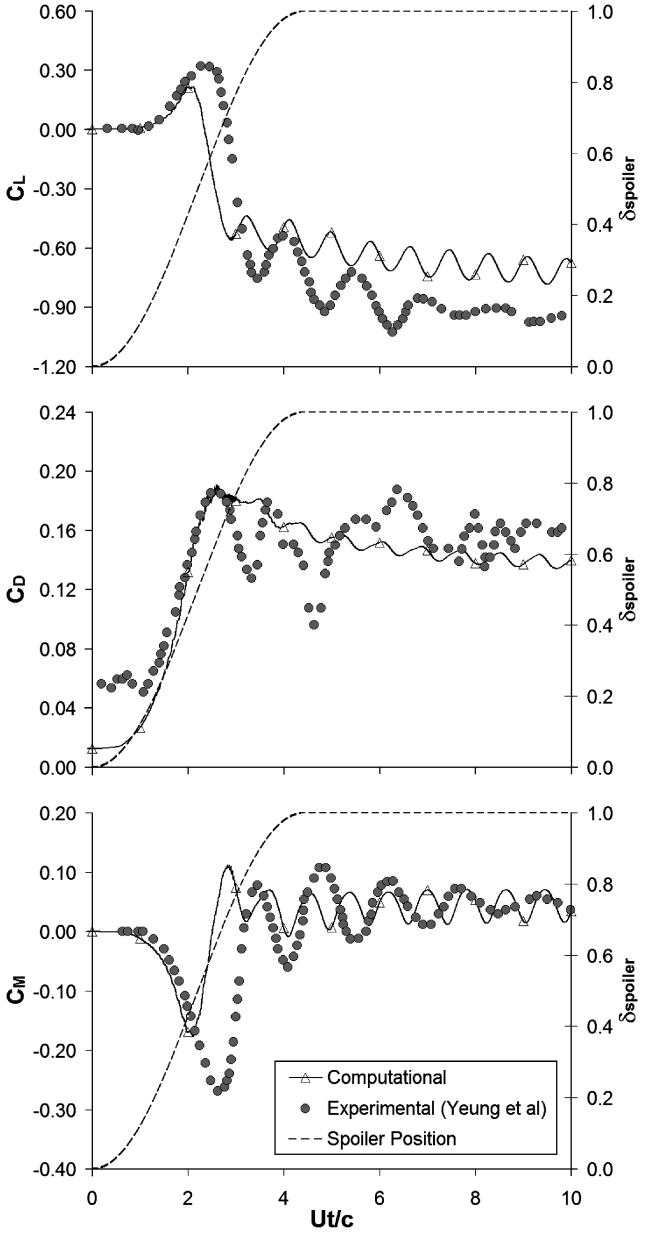

Fig. 7 Comparison of transient aerodynamic response between computational and experimental results for a deploying spoiler at $Re = 0.35 \times 10^6$ and $\alpha = 0$ deg.

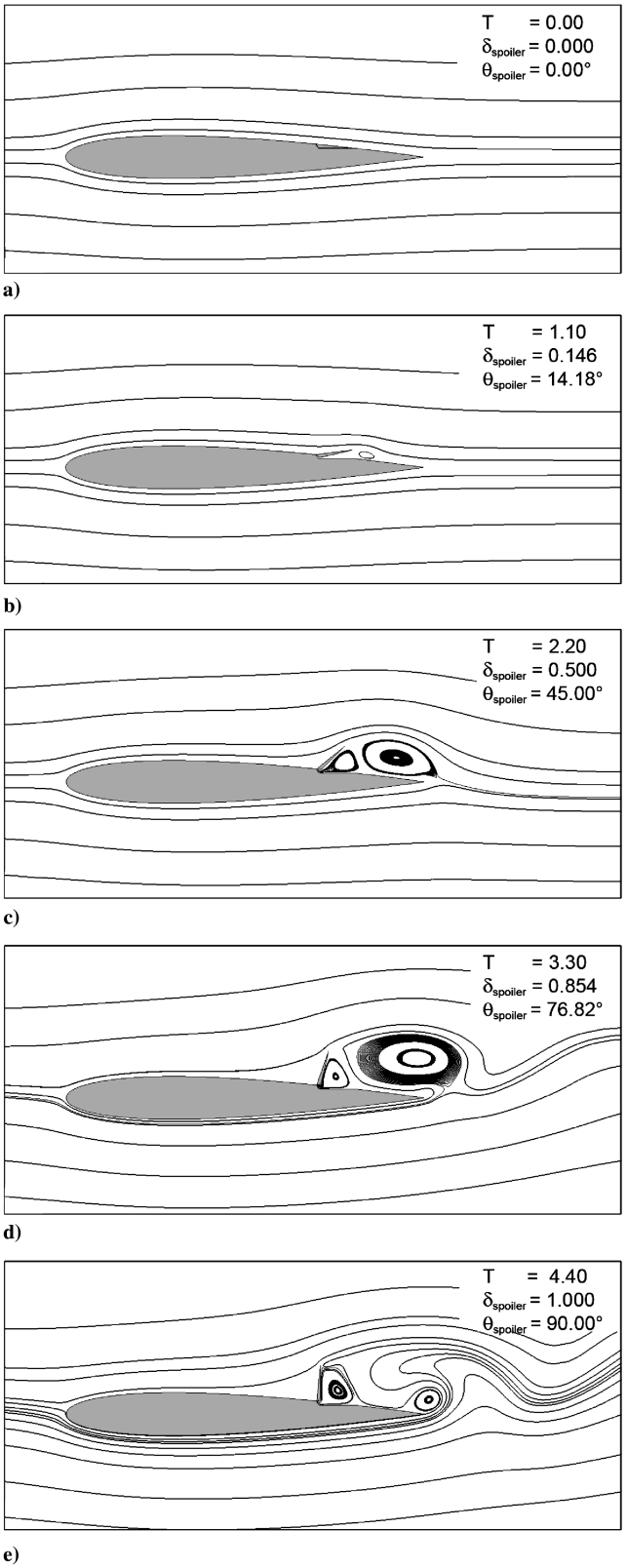

Fig. 8 Instantaneous streamlines at various times during spoiler deployment from onset $T = 0$ a) to completion $T = 4.4$ e).

experimental configuration. During the first half of deployment ($\sim 2c/U$) the computational predictions match experimental results closely.

The experimental peaks in lift and moment seen during deployment are not captured by the simulations. This difference indicates that the strong deployment roll-up vortex is shed slightly earlier in the computational simulation. This behavior may be due to a small hinge gap necessary in the computational simulation that had the effect of base venting the spoiler, accelerating the convection of the vortex, or possibly 3-D stall-type behavior occurs experimentally that the 2-D simulations are not modeling.

The shedding of this initial vortex stops the low pressure buildup behind the spoiler, accounting for the difference in lift and nose-up moment. In terms of spoiler position, the discrepancy of the initial peak (onset of shedding) is only about 5.4 deg, occurring approximately at $\theta_{\text{spoiler}} = 47.4$ deg experimentally and $\theta_{\text{spoiler}} = 42.0$ deg computationally. The small difference in the hinge gap geometry may have created enough base venting to accelerate the development and advection of this initial vortex.

Once the large buildup vortex is shed, a new vortex forms behind the spoiler and grows rapidly. As the counter-rotating vortices interact and shed, the lift drops and oscillates, while the pitching moment rises and begins to oscillate. Although the experiment shows a slow decay of the oscillations towards a steady state solution, the numerical solutions maintained a periodic oscillation and charac-

teristic amplitude. Nevertheless, the mean values of the oscillations for the pitching moment and drag are in excellent agreement with the experimental values. And overall, the computational results are in reasonable agreement with the experimental data, especially from a temporal perspective. Qualitatively, these results are completely consistent with both the experimental findings of Yeung et al. [22] and the computational results of Choi et al. [28].

Temporal Convergence

For time-accurate solutions to be valid, temporal accuracy must also be established. Because all time-marching schemes are based on solutions of previous steps, the convergence of those previous steps is critical. Without that convergence, solutions will diverge temporally. If the changes in the grid boundary conditions are small per time step, the solutions can still appear valid because the domain has not been greatly perturbed. This also implies that spatial residual will not reveal any problems either. So these dynamic time-accurate solutions require an additional convergence criterion beyond reducing the solution residual. With the requirement that the solution be converged at each global time step before continuing, temporal convergence can be measured in terms of the reduction of a solution residual per global time step (after a prescribed number of subiterations). In this study, the reduction of the RHS of L^2 norm residual is used specifically and will heretofore be referred to as the subiteration convergence. Because only the reduction per global time step is of concern, all measures of residual behave similarly.

Three factors determine the rate of convergence: the first is the size of the global time step, which is the temporal equivalent to the physical grid spacing, the second the number of solution iterations per global time step or subiterations, and finally the convergence rate of the solution on the physical grid. The convergence rate of the solution on the physical grid is a function of grid density, numerical scheme, and intergrid interpolation scheme; although by itself independent to time accuracy, it greatly affects the number of subiterations required to attain convergence at a particular time step.

In this study, the physical grid was kept fixed, while a variety of global time steps and subiteration combinations were examined. In performing an extensive convergence study, it was clear that both parameters must be adjusted and balanced for convergence. Low levels of temporal convergence (with subiteration convergence values of 0.01–0.5) led to solutions that appeared to have different time scales, clearly indicating temporal divergence, whereas L^2 norms of the residual showed nothing anomalous, all remaining low (with all grids showing 12–15 orders of magnitude convergence). Neither a large number (100–1000) of subiterations with a large time step ($DT = 0.1$) nor an extremely small time step ($DT = 10^{-6}$) with a low number of subiterations ($\sim$3) led to temporal convergence. Once subiteration convergence values of at least 1.5 were reached and sustained, solutions collapsed upon one temporal solution, with consistent temporal solutions for increasing subiteration convergence. For this problem, an optimal set of parameters was found to be 50 subiterations with $DT = 10^{-3}$. Because each grid has a different convergence rate, the lowest subiteration convergence (almost always for the finest near-body grid) value was used to provide the convergence criterion. The subiteration convergence of the two near-body grids and the first two off-body grid (BRICK) levels are shown in Fig. 9. The remaining off-body grids show even higher levels of convergence, ranging from 11 to 15 orders of magnitude of convergence per global iteration.

Validation Study Conclusions

From a methodology standpoint, the spoiler study was indispensable in providing unambiguous evidence of the importance subiteration convergence for temporal convergence, as well as providing guidance as to how to achieve that convergence. The primary unresolved issue with the study is the prediction of the shedding frequency; however, with the known issues of turbulence models and massive separation, this discrepancy is not unexpected. No matter how carefully the experimental study is designed and conducted, in real world flows, this massive separation and vortex breakdown is an unsteady 3-D phenomenon. So models using 2-D assumptions are disadvantaged; presumably, once computationally more practical for design type problems, detached-eddy simulation (DES) or even large-eddy simulation (LES) methodologies will improve the accuracy of predictions for these types of 3-D flows.

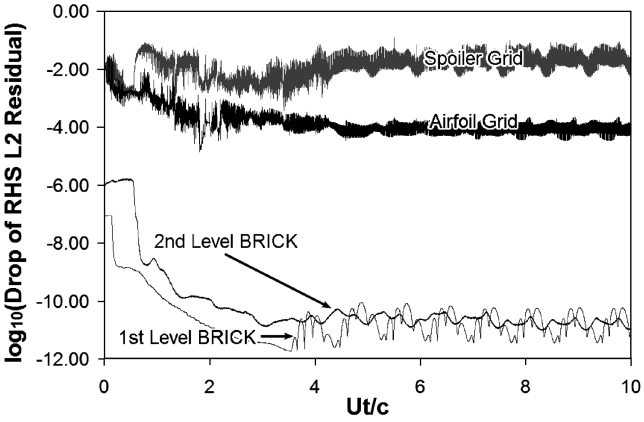

Fig. 9 Convergence per global iteration for near-body and first level BRICKS.

From a practical standpoint, however, the focus of the microtab study is not the steady state vortex shedding, but the dynamic temporal effects. It is clear from the validation study, that dynamic behavior during deployment can be accurately captured. In particular, this study lends a high level of support and confidence to the methodology for predicting time-accurate behavior of moving viscous surfaces. This validation, along with the static microtab study, has clearly shown that the present methodology can be used to accurately predict the unsteady behavior of the deploying microtab problem.

Results and Discussion

Baseline Microtab Deployment ($T_{\text{deploy}} = 1.00$ and $h_{\text{tab}} = 1.00\%c$)

The aerodynamic response for a $1.00\%c$ tab deployed in one nondimensional time unit ($T_{\text{deploy}} = 1.00$), at a 0 deg angle of attack is shown in Fig. 10. Time stations of interest are labeled (a)–(h), and corresponding surface pressure coefficient (C_P) plots and instantaneous streamlines at those same stations are shown in Figs. 11 and 12. The aerodynamic response over the first $50c/U$ after the onset of deployment along with their mean asymptotic values is shown in Fig. 13. A freestream Mach number of 0.25 and a Reynolds number (based on airfoil chord length) of 1.0×10^6 were used for all of the deploying microtab simulations. This configuration will be considered the baseline case for the microtab investigation. At standard atmosphere conditions, with a chord length, $c = 1$ ft, one nondimensional time unit would be equivalent to approximately 3.6 ms.

As the tab initially deploys a low pressure region and counter-clockwise vortex immediately forms behind the tab (Figs. 11b and 11c), increasing the drag on the airfoil. The corresponding low pressure region of the vortex behind the tab creates a down force - in the trailing edge region, generating a nose-up moment and reducing lift (Fig. 10). Up to station (d), the growing tab vortex behaves like a separation bubble. Until, eventually, the rear of the vortex reaches the trailing edge of airfoil (Fig. 12d), and the peak adverse lift and moment is reached (Fig. 10). Once the counter-clockwise vortex and its low pressure region extend beyond the trailing edge, a very interesting phenomenon occurs. Some of the upper surface flow leaving the trailing edge is entrained into this lower surface vortex. But it is the behavior of the slower upper surface boundary-layer flow that is most interesting. This flow is pulled down around the trailing edge and pushed upstream along the lower surface by the main vortex (Fig. 12d). This flow continues upstream along the lower surface, driven by the vortex, and travels down the suction side of the tab to the lower tip of the tab. It continues along the lower surface of the tab (approximately halfway) before

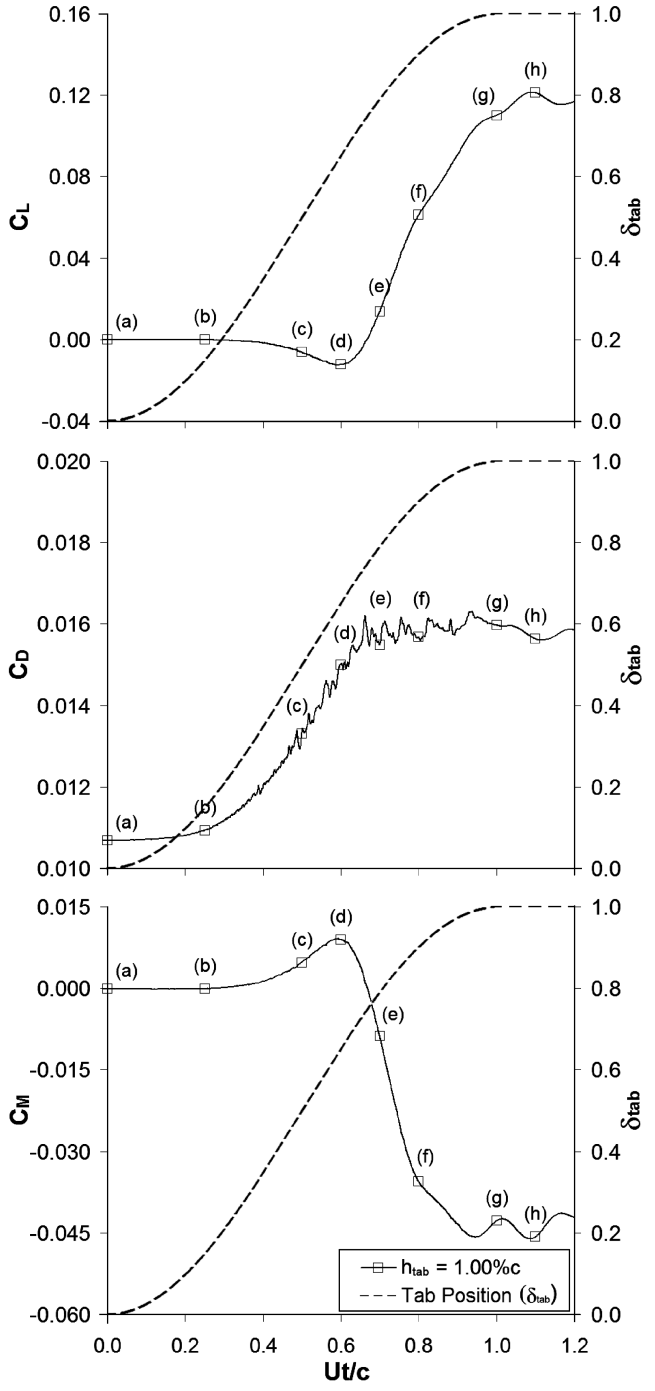

Fig. 10 Transient lift, drag, and pitching moment response during tab deployment. Baseline: $Ma = 0.25$, $Re = 1 \times 10^6$, $\alpha = 0$ deg, $1.00c/U$ deployment, and $1.00\%c$ tab.

meeting lower surface flow that has traveled along the pressure side of the tab. Here, at this new stagnation point, the two flows leave the airfoil/tab surface. This shift in the separation point from the trailing edge to the tip of the tab changes the Kutta condition of the airfoil. This change effectively increases the camber of the aerodynamic profile and circulation generation. Once this occurs, the trend in the adverse lift and moment is reversed, and those values begin to climb (Fig. 10).

From an inviscid flow point of view, it can also be argued that the new stagnation point is aft of the tab vortex. And that the effective increase in camber is due to the increase in lower surface trailing edge thickness from the tab vortex.

The aerodynamic response is remarkably rapid, with a significant portion occurring during the tab deployment. Expectedly, the drag

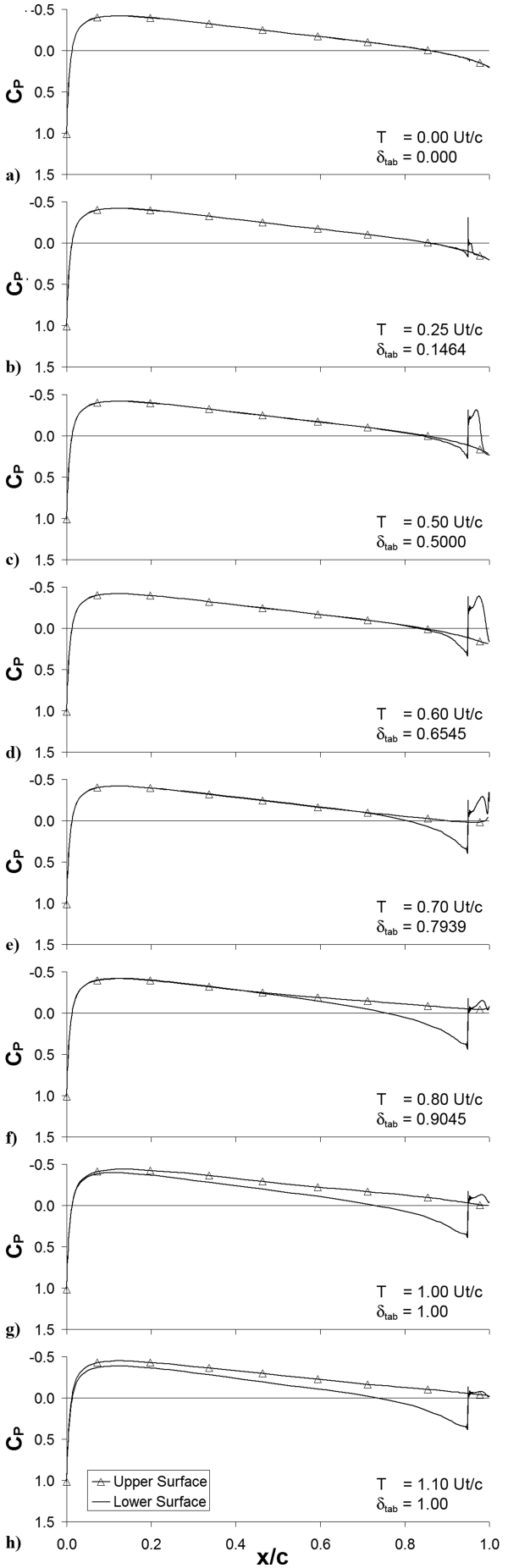

Fig. 11 Surface (including tab lower surface) C_P plots during baseline tab deployment. a)–h) correlate with labels in Fig. 10.

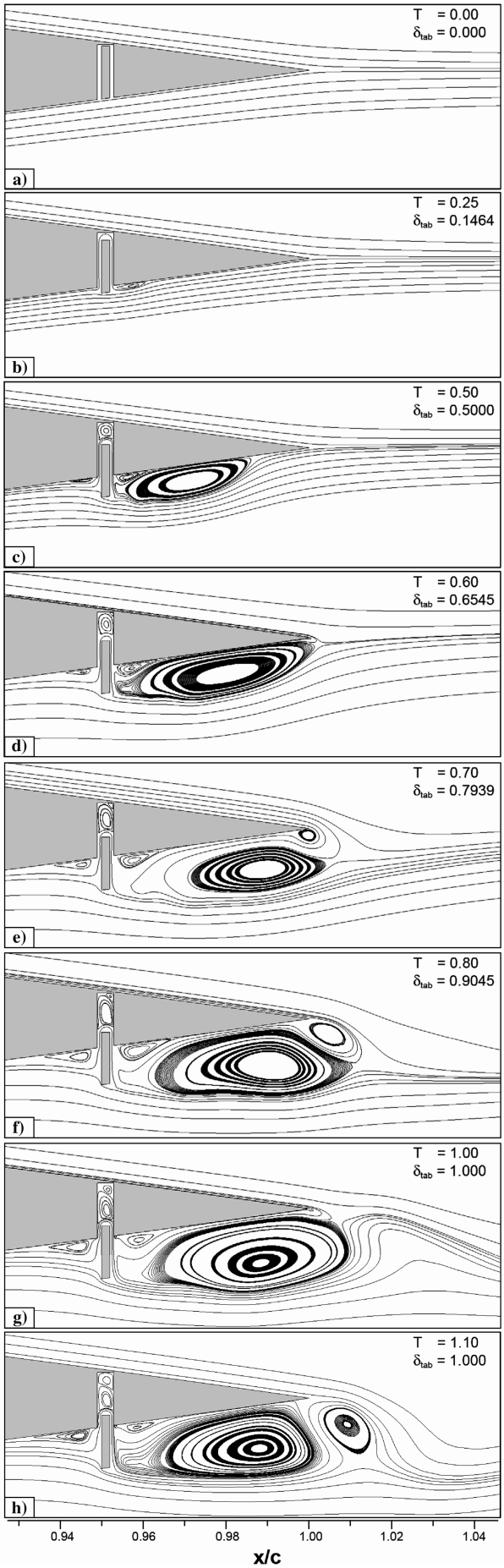

Fig. 12 Instantaneous streamlines in tab region during baseline tab deployment. a)–h) correlate with labels in Fig. 10.

increase, more than 90% of which was pressure drag, responded immediately with tab deployment. Post deployment, the high frequency drag oscillations also disappear; it is unclear what causes these oscillations. Almost immediately post deployment, a harmonic shedding at approximately 7.79 cycles/(c/U) (or 2200 Hz for $c =$ 1 ft at standard atmosphere) is established.

The aerodynamic responses asymptotically approach mean steady state values at noticeably different rates (Fig. 13). The pitching moment, dominated by pressure, quickly reaches a mean steady state value within $1c/U$ post deployment, while the drag does not reach a steady mean until $\sim 10c/U$ post deployment. The lift rapidly climbs over the initial $\sim 5c/U$, before climbing to 90% of the mean asymptotic lift another $\sim 10c/U$ later. The asymptotic lift value of $C_{L,\infty} = 0.208$ is determined using an extrapolation of a least squares exponential curve fit of the lift response. By $T = 50$, a mean lift of 0.2068 or 99.5% of the asymptotic value is reached.

Although it is the change in the Kutta condition that creates the initial jump in lift during deployment, it is a slower shift in the leading edge stagnation point, as the pressure field and circulation of the

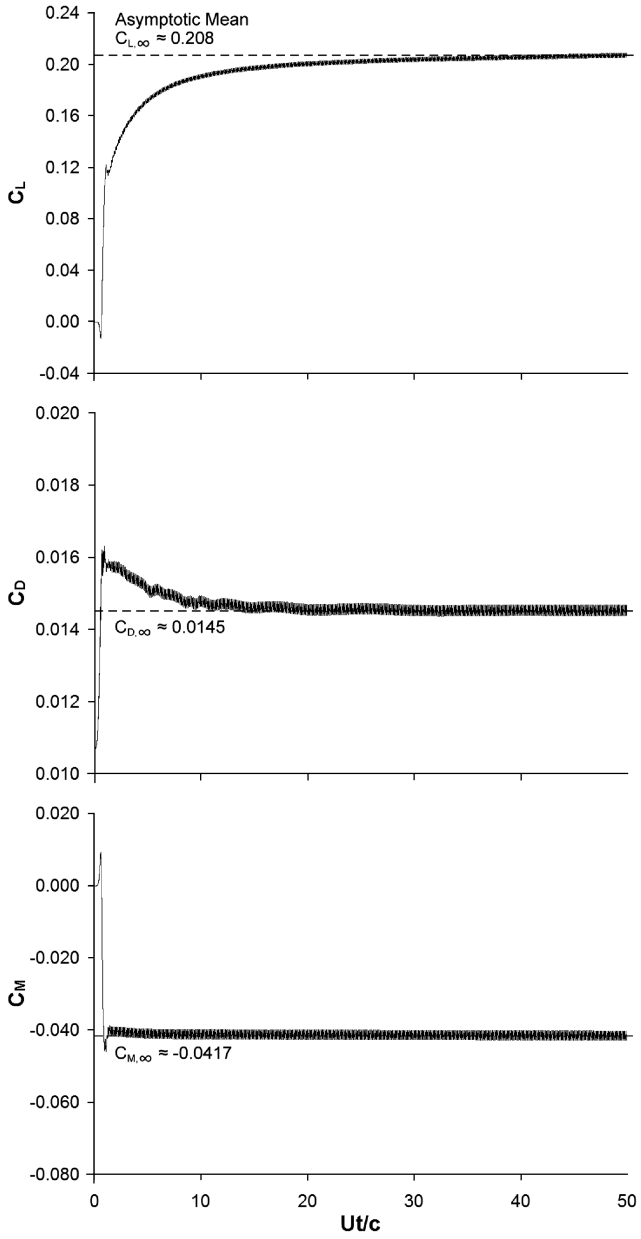

Fig. 13 Transient lift, drag, and pitching moment response asymptotically approaching steady mean solution. Baseline: $Ma = 0.25$, $Re = 1 \times 10^6$, $\alpha = 0$ deg, $1.00c/U$ deployment, and $1.00\%c$ tab.

entire domain around the airfoil adjusts that generates the increase in lift over the remainder of the simulation.

The time-accurate calculation was started from a converged solution for the retracted tab configuration. This calculation was run a full nondimensional time step ($1c/U$), time accurately, with a retracted tab to advect any transients from the airfoil surface. Because of the smaller time scales, all the microtab time-accurate calculations used a conservative nondimensional time step of $DT = 1 \times 10^{-4}$. During deployment, 50 dual-time stepping subiterations were used to achieve over 2 orders of magnitude of subiteration convergence. Solutions using various time steps between 1×10^{-3} and 5×10^{-5} created no qualitative temporal difference in solutions.

A grid convergence study was also performed for this baseline case. Two additional grid densities were examined. The first doubled whereas the second cut in half the number of grid points in all of the near-body grids (all grids in Fig. 2). Both new grid configurations were run using the baseline deployment parameters, with a time step of $DT = 1 \times 10^{-4}$ and 50 subiterations for $2c/U$.

The finer grid displayed a lower level of subiteration convergence compared to the baseline grid; however, it still reached approximately 1 order of magnitude of subiteration convergence. The solution matched the baseline solution extremely well, essentially overlapping the baseline results.

The reduced grid point configuration displayed much faster subiteration convergence than the baseline grid, with over 4 orders of magnitude convergence using the same time advancement parameters. In terms of the magnitude of the coefficients, the solution displayed small oscillations ($\sim$0.001 for C_L and $\sim$0.0001 for C_D) that quickly resettled on the baseline solution. Overall, this solution showed excellent agreement in the mean with the baseline solution, with essentially an identical temporal response. This study also showed the effects of the spatial convergence rates of the underlying grid affecting the rate of temporal convergence.

The grid independence study clearly shows that the baseline grid was sufficient to accurately resolve the entire flow domain. Moreover, with the difference levels of subiteration convergence, the agreement with the baseline solution provided additional temporal validation.

Deployment Time Study ($h_{\text{tab}} = 1.00\%c$)

In this study, the effect of deployment time was examined. The deployment height was fixed at the baseline $1.00\%c$, so that here the tab velocity profile was scaled to generate the baseline displacement for desired deployment times. Tab deployment times (T_{deploy}) of 0.25, 0.50, 0.75, 1.00, 1.50, and 2.00 were examined. The aerodynamic responses for the various deployment times are shown in Fig. 14. The lift response characteristics are summarized and compared in Table 1. Using the asymptotic mean lift coefficient ($C_{L,\infty} = 0.208$) for the baseline $1.00\%c$ tab configuration, a time to half lift $T_{50\%}$ or an effective rise time was defined. Because the purpose of the $T_{50\%}$ parameter is only to illustrate the lift response trend, and due to the highly oscillatory nature of the lift curves, the nondimensional time that each case initially reached $C_{L,50\%} = 0.104$ was defined as $T_{50\%}$.

As expected, the shorter deployment times generated a larger adverse response in lift and moment than longer deployment times. In fact, for deployment times shorter than the baseline, the drag also exhibits adverse behavior as a spike in magnitude. Although the peak adverse lift and 50% lift occurred earlier with faster tab deployment, when normalized by deployment time, the trend is reversed. With deployment times of $2.00c/U$ the adverse response becomes almost negligible ($C_{L,\text{adverse}} = -0.0047$). However, the most interesting behavior from this study is that even with all of the different transient effects during deployment, at $T = 2$, all the cases reached approximately the same aerodynamic state in terms of lift, drag, and pitching moment. Presumably, slightly slower deployments would generate no adverse responses at all, showing a quasisteady behavior. Most importantly, this study does show that the transients during deployment do not have a significant effect on the development of flow post deployment.

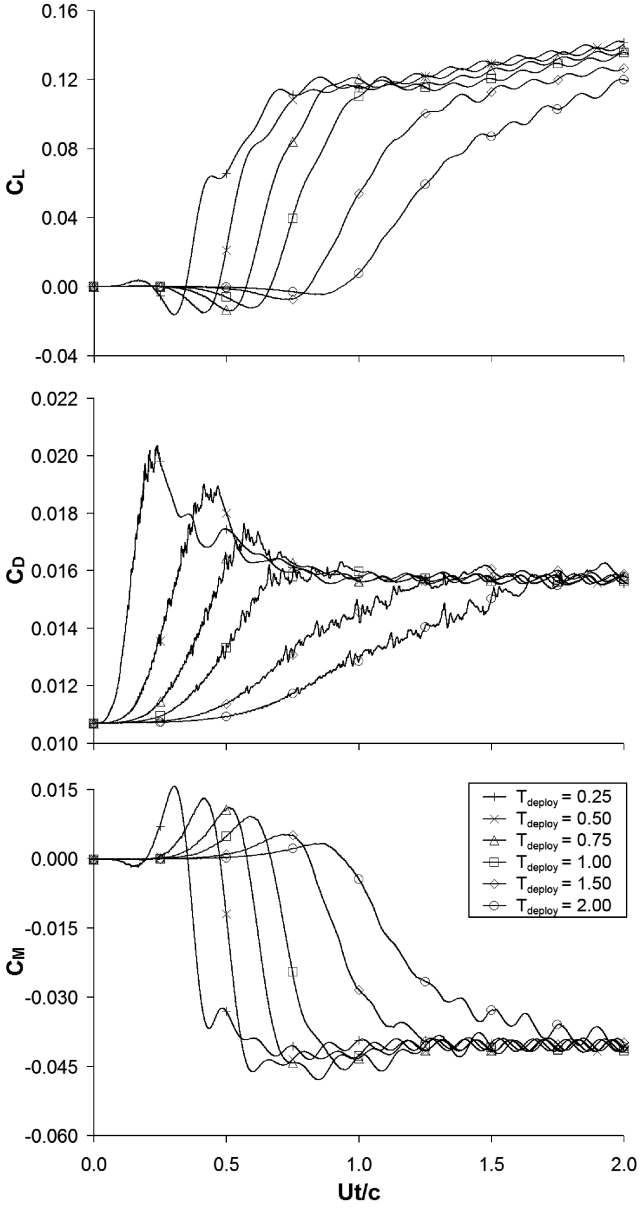

Fig. 14 Transient aerodynamic responses of varying deployment times: $T_{\text{deploy}} = 0.25, 0.50, 0.75, 1.00, 1.50$, and 2.00 ($h_{\text{tab}} = 1.00\%c$, $\alpha = 0$ deg).

Table 1 Comparison of peak adverse lift, delay times, and rise times for various deployment times

T_{deploy}	$C_{L,\text{adverse}}$	T_{delay}	$T_{\text{delay}}/T_{\text{deploy}}$	$T_{50\%}$	$T_{50\%}/T_{\text{deploy}}$
0.25	−0.0164	0.303	1.212	0.647	2.589
0.50	−0.0156	0.412	0.824	0.724	1.447
0.75	−0.0143	0.507	0.676	0.824	1.099
1.00	−0.0126	0.593	0.593	0.946	0.946
1.50	−0.0076	0.716	0.477	1.329	0.886
2.00	−0.0047	0.836	0.418	1.697	0.848

Tab Height Study ($T_{\text{deploy}} = 1.00$)

In this study, the effect of final deployment height was examined. The deployment time was fixed at the baseline $T_{\text{deploy}} = 1.00$, so that the tab velocity profile was scaled in each case to generate the desired tab displacement. Tab heights of 0.50, 0.75, 1.00, and 1.20%c were examined. The aerodynamic responses for the various tab heights are shown in Fig. 15. As expected, the larger deployment heights yielded larger increases in lift post deployment, with the 1.20%c tab generating more than 3 times the lift of the 0.50%c tab at the end of deployment. For all tab heights, the drag response was very similar, responding uniformly to tab height, with taller tab heights creating more drag. Using the mean post deployment ($1–2c/U$) values for lift, drag, and moment, the incremental changes were nearly linearly proportional to tab heights between 0.50–1.00%c. However, this linear relationship did not hold at tab height of 1.20%c, where drag increased at a higher rate and lift and moment changing at a lower rate relative to tab height.

Although the responses all asymptotically approach steady values as physical time progresses like the baseline case, the differences between the cases for all three aerodynamic coefficients remain constant post deployment. Expectedly, shedding frequency increases with decreasing tab height; however, for the shortest (0.5%c) tab, the shedding frequencies damp out almost immediately after one or two cycles post deployment. Because for all four cases the same deployment time was used, each tab was deployed with a different velocity. This may account for the difference in time when peak adverse lift occurs.

Angle of Attack Study ($T_{\text{deploy}} = 1.00$ and $h_{\text{tab}} = 1.00\%c$)

In this study, the effect of the freestream angle of attack was examined. The deployment was fixed at the baseline parameters. Angles of attack of $\alpha = -8, -4, 0, 4$, and 8 deg were examined. The aerodynamic responses for the baseline deployment at various airfoil angles of attack are shown in Fig. 16. For clarity, the change in lift due to tab deployment, $\Delta C_L = C_L - C_{L,\text{retract}}$, is shown in Fig. 16, where $C_{L,\text{retract}}$ is -0.848 at $\alpha = -8$ deg, -0.434 at $\alpha = -4$ deg, 0.000 at $\alpha = 0$ deg, 0.436 at $\alpha = 4$ deg, and 0.850 at $\alpha = 8$ deg. Note the slight asymmetry in the lift with angle attack is a result of the small change in the flowfield created by the retracted tab and cavity.

In terms of lift, the lift increment (ΔC_L) generated from tab deployment clearly improves with increasing angles of attack. The

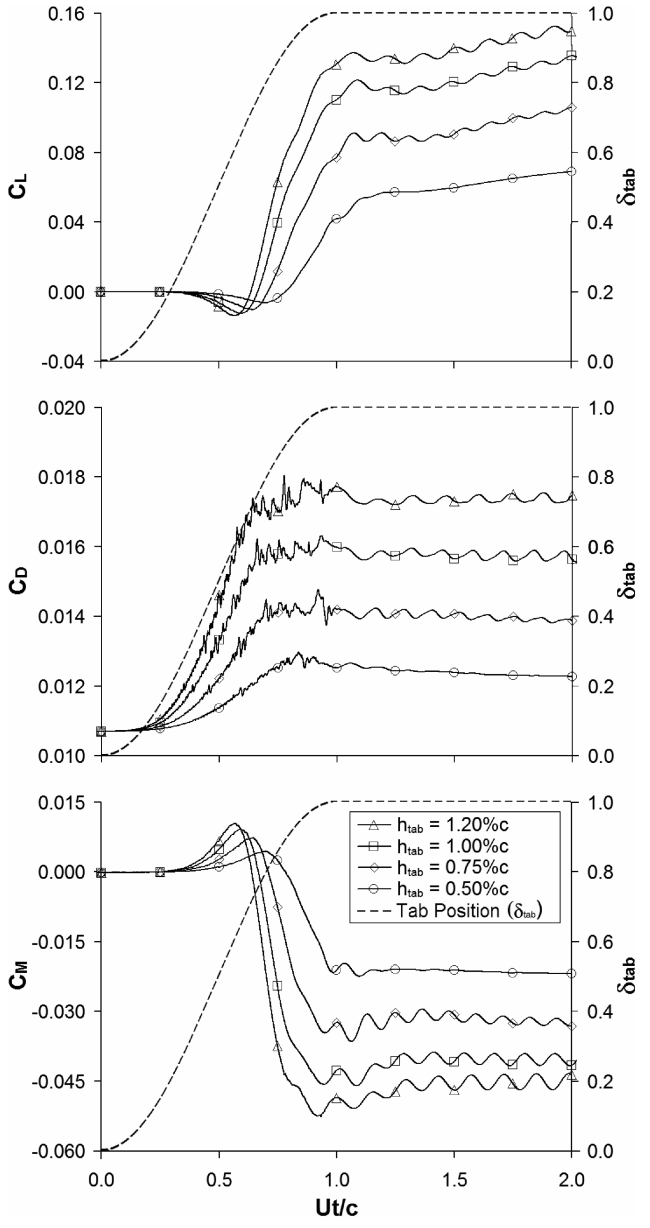

Fig. 15 Transient aerodynamic responses of varying tab deployment heights: $h_{\text{tab}} = 0.50, 0.75, 1.00$, and 1.20%$c$ ($T_{\text{deploy}} = 1.00, \alpha = 0$ deg).

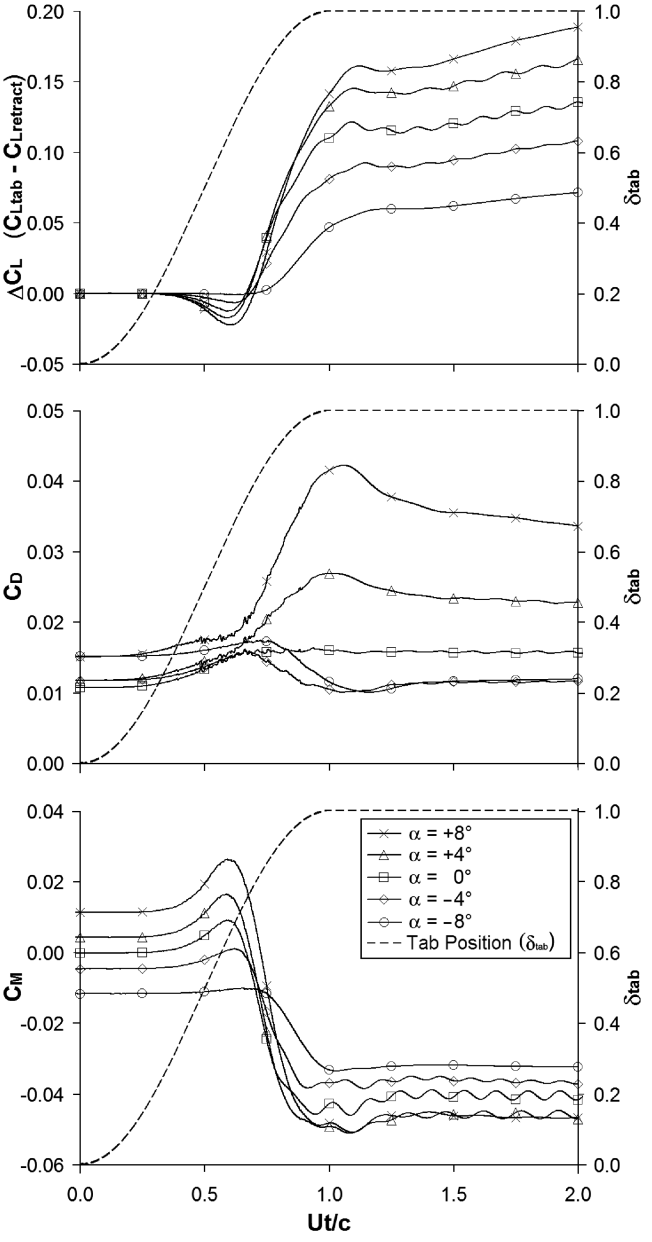

Fig. 16 Transient aerodynamic responses of baseline tab deployment ($T_{\text{deploy}} = 1.00$, $h_{\text{tab}} = 1.00\%c$) at $\alpha = -8, -4, 0, 4$, and 8 deg.

difference is fairly dramatic, with the $\alpha = 8$ deg generating almost 3 times as much lift at $T = 2$ compared to the $\alpha = -8$ deg case. Physically, this is due to changes in the boundary-layer thickness with angle of attack and, hence, the ratio of tab height to boundary-layer thickness. With increasing angle of attack, the lower surface boundary layer decreases in thickness due to the more favorable pressure gradient, whereas decreasing angle of attack increases that thickness due to the more adverse pressure gradient.

In addition to the effects on lift, there also appears to be a large drag penalty when the tab is deployed at positive angles of attack as well. The change in pressure drag accounts entirely for this increase; as tab deploys into a thinner (compared to the baseline) boundary layer, the total base drag increases. However, at negative angles of attack, tab deployment actually appears to slightly reduce drag. This drag reduction (at least initially after deployment) occurs because the upper surface boundary-layer thickness is actually reduced by the trailing edge suction effect of the lower surface tab. Additionally, there is a smaller pressure drag penalty as the tab deploys into the thicker (at negative angles of attack) lower surface boundary layer. Finally, due to a separated region behind the tab, viscous drag (which is ~0.008 predeployment) drops by ~5% after the tab is deployed. So the net gain is actually a drag reduction.

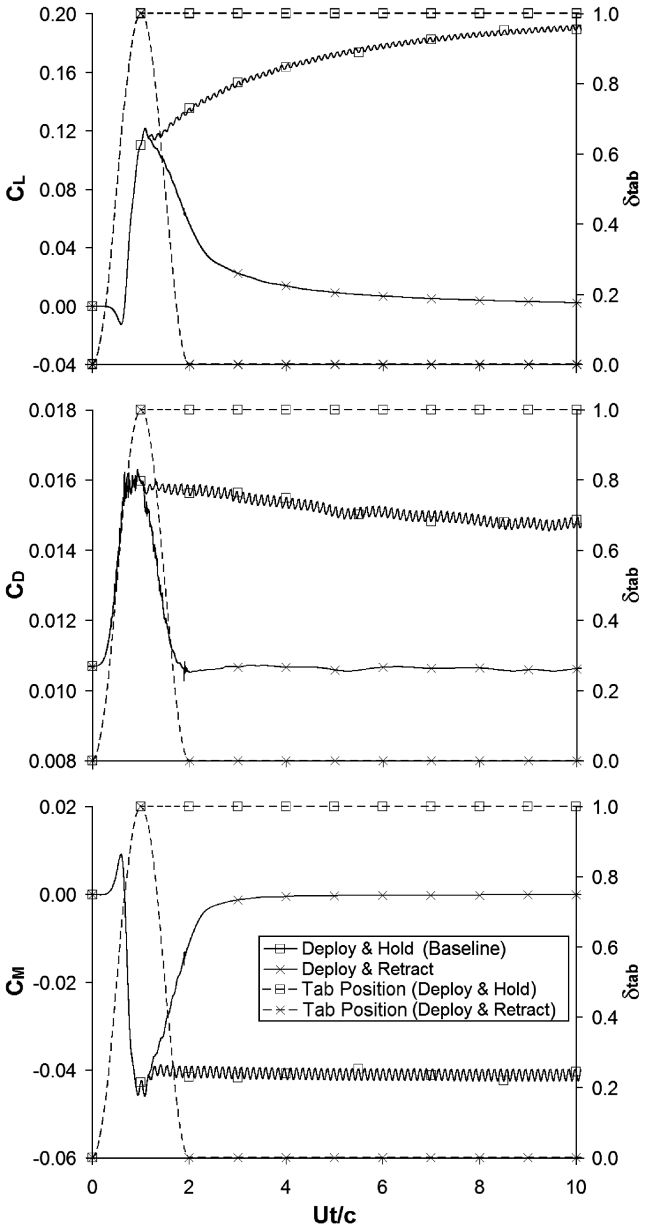

Fig. 17 Transient aerodynamic responses of a tab deployment and retraction with a baseline deployment only profile ($h_{\text{tab}} = 1.00\%c$, $\alpha = 0$ deg).

The pitching moment showed similar behavior to lift, with increasing response with increase angles of attack. In fact the predeployment pitching moment ranking is effectively completely reversed post deployment. In fact, at $\alpha = 4$ and 8 deg orientation of the pitching moment is reversed from a nose-up to a nose-down moment.

Temporally, the responses were very similar, with the peak adverse lift all occurring near $T = 0.6$, with the exception of the -8 deg case which did not generate any adverse lift. It is also interesting to note that compared to the baseline, the shedding amplitude is reduced at ± 4 deg and shedding is eliminated at ± 8 deg.

Tab Retraction Study ($T_{\text{deploy}} = 1.00$ and $h_{\text{tab}} = 1.00\%c$)

In this study, the transient response of a tab retraction is examined. The deployment was fixed at the baseline parameters; however, as opposed to the deploy and hold profile of the baseline case, the tab was retracted by reversing the deployment velocity profile. The aerodynamic responses for the baseline deployment and the deploy and retract profile are shown in Fig. 17.

The retraction response times correlated well with the response times during deployment. The initial response of the lift was fast, with lift dropping $\sim 0.12c/U$ after the onset of retraction, and dropping almost to half the peak value at the end of the tab retraction. Once the tab is retracted, the change slowed significantly, only returning to a predeployment state almost $6c/U$ later. Again, the drag reacts almost immediately with the tab position, reaching a predeployment value almost as soon as the tab is retracted. The pitching moment lags the drag response very slightly, but still reaches the predeployment moment within $3c/U$ after retraction. There were also no adverse spikes or other transient phenomenon that occurred with the retraction.

Conclusion

With the extensive and comprehensive validation work performed for this study, the confidence in the results is reasonably high. Two external validation studies were performed. The first case using a static microtab ensured the capability to capture microtab generated flow. The second using the deploying spoiler ensured the capability to capture unsteady flow around moving viscous surface accurately. Furthermore, the internal consistency of the methods was rigorously demonstrated with grid independence, time step, and subiteration studies.

This investigation demonstrated the flow transients during deployment of microtab under various conditions. It was shown that microtabs have a rapid initial response during deployment of approximately half the mean steady state lift, before asymptotically reaching 90% of that mean $10c/U$ (or ~0.036 s for $c = 1$ ft) later. It was also shown that the tabs produce negligible adverse responses for deployments in $1c/U$ or greater, and modest adverse responses ($C_{L,\text{adverse}} \approx 0.01$–$0.025$) for faster deployments. This study has clearly shown that there are no unexpected deployment effects that make microtabs any less attractive as active load control devices.

For future work, the deploying microtab applied to other airfoils in different flow conditions, potentially for rotorcraft or wind turbine applications, will be examined. The effect of the cavity will be examined, by deploying a tab flush from the surface. Although in terms of an actual physical device, the cavity configuration would be a more accurate model. The cavity might also be behaving like a base vented spoiler, accelerating the development and advection of the initial transients.

Acknowledgments

The authors would like to thank the National Defense Science and Engineering Graduate Fellowship and the Army Research Office for support during this and ongoing efforts. We would also like to thank Sandia National Laboratories (Dale Berg and Jose Zayas) for support

during the early phases of this study and providing additional computational resources.

References

[1] Liebeck, R. H., "Design of Subsonic Airfoils for High Lift," *Journal of Aircraft*, Vol. 15, No. 9, Sept. 1978, pp. 547–561.

[2] Yen, D. T., van Dam, C. P., Bräeuchle, F., Smith, R. L., and Collins, S. D., "Active Load Control and Lift Enhancement Using MEM Translational Tabs," AIAA Paper 2000-2422, June 2000.

[3] Yen-Nakafuji, D. T., van Dam, C. P., Smith, R. L., and Collins, S. D., "Active Load Control for Airfoils Using Microtabs," *Journal of Solar Energy Engineering*, Vol. 123, No. 4, Nov. 2001, pp. 282–289.

[4] Standish, K. J., "Aerodynamic Analysis of Blunt Trailing Edge Airfoils & A Microtab-Based Load Control System," M.S. Thesis, University of California, Davis, Dec. 2003.

[5] Standish, K. J., and van Dam, C. P., "Computational Analysis of a Microtab-Based Aerodynamic Load Control System for Rotor Blades," *Journal of American Helicopter Society*, Vol. 50, No. 3, July 2005, pp. 249–258.

[6] Mayda, E. A., van Dam, C. P., and Yen-Nakafuji, D. T., "Computational Investigation of Finite Width Microtabs for Aerodynamic Load Control," AIAA Paper 2005-1185, Jan. 2005.

[7] Buning, P. G., Jespersen, D. C., Pulliam, T. H., Chan, W. M., Soltnick, J. P., Krist, S. E., and Renze K. J., OVERFLOW User's Manual, Ver. 1.8ab, NASA Langley Research Center, July 2003.

[8] Jespersen, D. C., Pulliam, T. H., and Buning, P. G., "Recent Enhancements to OVERFLOW," AIAA Paper 97-0644, Jan. 1997.

[9] Beam, R., and Warming, R., "An Implicit Factored Scheme for the Compressible Navier-Stokes Equations," *AIAA Journal*, Vol. 16, No. 4, 1978, pp. 393–402.

[10] Menter, F., "Two-Equation Eddy-Viscosity Turbulence Models for Engineering Applications," *AIAA Journal*, Vol. 32, No. 8, 1994, pp. 1598–1605.

[11] Bardina, J. E., Huang, P. G., and Coakley, T. J., "Turbulence Modeling, Validation, Testing and Development," NASA TM-110446, Apr. 1997.

[12] Kral, L. D., Mani, M., and Ladd, J. A., "Application of Turbulence Models for Aerodynamic and Propulsion Flowfields," *AIAA Journal*, Vol. 34, No. 11, Nov. 1996, pp. 2291–2298.

[13] Pandya, S. A., Venkateswaran, S., and Pulliam, T. H., "Implementation of Precondition Dual-Time Procedures in OVERFLOW," AIAA Paper 2003-0072, Jan. 2003.

[14] Nichols, R. H., and Heikkinen, B. D., "Validation of Implicit Algorithms for Unsteady Flows Including Moving and Deforming Grids," AIAA Paper 2005-0683, Jan. 2005.

[15] Steger, J. L., Dougherty, F. C., and Benek, J. A., "A Chimera Grid Scheme," *Advances in Grid Generation*, edited by K. N. Ghia and U. Ghia, ASME FED, Vol. 5, ASME, New York, 1983, pp. 59–69.

[16] Chan, W. M., Rogers, S. E., Nash, S. M., Buning, P. G., and Meakin, R. L., User's Manual for Chimera Grid Tools, Ver. 1.8, NASA Ames Research Center, May 2003.

[17] Chan, W. M., "The OVERGRID Interface for Computational Simulations on Overset Grids," AIAA Paper 2002-3188, June 2002.

[18] Chan, W. M., Gomez, R. J., Rogers, S. E., and Buning, P. G., "Best Practices in Overset Grid Generation," AIAA Paper 2002-3191, June 2002.

[19] Meakin, R. L., "Automatic Off-Body Grid Generation for Domains of Arbitrary Size," AIAA Paper 2001-2536, June 2001.

[20] Murman, S. M., Chan, W. M., Aftosmis, M. J., and Meakin, R. L., "An Interface for Specifying Rigid-Body Motions for CFD," AIAA Paper 2003-1237, Jan. 2003.

[21] Meakin, R. L., "Object X-Rays for Cutting Holes in Composite Overset Structured Grids," AIAA Paper 2001-2537, June 2001.

[22] Yeung, W. W. H., Xu, C., and Gu, W., "Reduction of Transient Adverse Effects of Spoilers," *Journal of Aircraft*, Vol. 34, No. 4, July–Aug. 1997, pp. 478–484.

[23] Meakin, R. L., and Wissink, A. M., "Unsteady Aerodynamic Simulation of Static and Moving Bodies Using Scalable Computers," AIAA Paper 99-3302, July 1999.

[24] Buning, P. G., Gomez, R. J., and Scallion, W. I., "CFD Approaches for Simulation of Wing-Body Stage Separation," AIAA Paper 2004-4838, Aug. 2004.

[25] Saephan, S., van Dam, C. P., Fremaux, C. M., DalBello, T., "Simulation of Flow About Rotating Forebodies at High Angles of Attack," *Journal of Aircraft*, Vol. 41, No. 6, Nov.–Dec. 2004, pp. 1298–1305.

[26] Strawn, R. C., and Djomehri, J. M., "Computational Modeling of Hovering Rotor and Wake Aerodynamics," *Journal of Aircraft*, Vol. 39, No. 5, Sept.–Oct. 2002, pp. 786–793.

[27] Baker, J. P., Standish, K. J., and van Dam, C. P., "Two-Dimensional Wind Tunnel and Computational Investigation of a Microtab Modified S809 Airfoil," AIAA Paper 2005-1186, Jan. 2005.

[28] Choi, S. W., Chang, K. S., and Ok, H., "Parametric Study of Transient Spoiler Aerodynamics with Two-Equation Turbulence Models," *Journal of Aircraft*, Vol. 38, No. 5, Sept.–Oct. 2001, pp. 888–894.